Journal of The Electrochemical Society, 2022 **169** 063507
1945-7111/2022/169(6)/063507/10/$40.00 © 2022 The Electrochemical Society ("ECS"). Published on behalf of ECS by IOP Publishing Limited

Finite Element Modeling of Electrochemical Polishing of Niobium in Hydrofluoric-Sulfuric Acid Electrolyte

Kaiwen Wang,[1] Wenjun Cai,[1,z] Hui Tian,[2,z] and Charles E. Reece[2,z]

[1] *Department of Materials Science and Engineering, Virginia Polytechnic Institute and State University, Blacksburg, Virginia 24061, United States of America*
[2] *Thomas Jefferson National Accelerator Facility, Newport News, Virginia 23606, United States of America*

Niobium (Nb) used in superconducting radio-frequency cavities requires smooth surface to achieve optimal performance. In this work, a finite element model that coupled electrochemistry, heat transfer, and fluid dynamics was developed to investigate the electrochemical polishing mechanisms of Nb, using experimentally measured polarization results of coupon samples as validations. The current and potential distribution, oxide growth kinetics of Nb in a complex cavity geometry was investigated as a function of temperature and coolant flow. A low temperature coolant with intermediate flow rate was found to reduce surface current and ensure oxide uniformity. These results could shed light on the design of future particle accelerators.

[DOI: 10.1149/1945-7111/ac7354]

Manuscript submitted March 8, 2022; revised manuscript received May 3, 2022. Published June 10, 2022.

Superconducting radio-frequency (SRF) cavities are critical components for particle accelerators, which exploit high resonant electric fields to accelerate charged particles.[1] To achieve desired accelerating performance, niobium (Nb) SRF cavities require microscopically smooth internal surface at the grain level since the SRF current flows in the outmost ~40 nm of the surface.[2] Traditional chemical etching fails at producing grain-level smoothness due to the differences of etching rate at grain interior vs grain boundaries, as well as grains with different crystallographic orientation. For example, buffered chemical polishing treatments of Nb result in a typical root mean square surface roughness of about 1.6 ± 0.42 μm.[3] Electrochemical polishing, on the other hand, overcomes such limitations by controlling metal dissolution rate at the limiting current range so that a uniform surface can be achieved.[4] When metals dissolves at the limiting current density, the dissolving metal (e.g. Nb) surface is typically covered by a thin compact solid film consisting of an oxide (e.g. Nb_2O_5), perhaps contaminated with significant amounts of anion from the electrolyte, as shown by previous surface characterizations.[5,6] If the ionic conductivity of the film is sufficient to allow for the passage of the anodically formed cations at high rate, the dissolution/removal of atoms from the metal into the solid film would then occur with no dependence on local polarization potential, producing a smooth surface regardless of the microstructure (e.g. crystallographic orientation and grain boundaries) of the metal, since it is governed by the availability of cation vacancies in the film and not by the lattice position of the metal atoms.[4,7–9]

Past experimental studies show that electrochemical polishing of Nb SRF cavity surface (Fig. 1a) using an electrolyte of concentrated sulfuric acid (98%) and hydrofluoric acid (49%) by a volume ratio of 10:1 result in smooth Nb surfaces.[4,9] While many studies[9–11] utilize acidic fluoride electrolyte since HF is effective in dissolving the anodic films on Nb, those using fluoride-free electrolyte has also been reported.[8,12,13] Studies investigating the mechanisms and kinetics of the electrochemical reactions during the electrochemical polishing of the Nb has been conducted by several groups, such as Guan et al.[14] and Hryniewicz et al.[5] X-ray photoelectron spectroscopy (XPS) confirmed the existence of the intermediate state of Nb_2O_5 and NbF_5. The mechanism involving the formation of Nb_2O_5 by anodic polarization and dissolution of the oxide layer under the influence of HF is also confirmed by electrochemical impedance spectroscopy (EIS) study.[15] Based on these results, the electrochemical polishing process of the Nb could be separated into two steps, as shown schematically in Fig. 1b. Firstly, the applied potential drives the Nb to anodize and form a thin oxide layer of niobium pentoxide (Nb_2O_5), which could be expressed by the reaction:

$$2Nb + 5H_2O \rightarrow Nb_2O_5 + 10H^+ + 10e^-, \qquad [1]$$

while at the same time, the hydrogen evolution reaction happens at the Al surface of the counter electrode:

$$2H^+ + 2e^- \rightarrow H_2. \qquad [2]$$

The second part of the process involves the dissolution of the niobium pentoxide at the electrode-electrolyte interface due to the synergistic effect of H^+ and F^- ions:

$$Nb_2O_5 + 10H^+ + 10F^- \rightarrow 2NbF_5 + 5H_2O. \qquad [3]$$

The NbF_5 converts to a dissolvable state of $[NbF_7]^-$ in the presence of hydrofluoric acid (HF). The thickness of the Nb_2O_5 layer is determined by the formation of Nb_2O_5, which is affected by the applied potential and the dissolution of the Nb_2O_5. With higher applied potential, the oxidation rate will increase while the dissolution rate of the Nb_2O_5 has an upper limit due to the diffusion-limited mass transport control of fluorine ions. This results in thicker Nb_2O_5 layer, reduces the electropolishing current and slows down the oxidation rate, which will eventually become the same as the dissolution rate. The thickness of the Nb_2O_5 layer and the current density then reaches a steady state. A voltage range exists within which, the increase in applied voltage does not increase the current density so that the electrochemical polishing proceeds in a controlled rate, which is referred to as the plateau region.[16,17] Once the overpotential on the cavity is maintained in the plateau region to allow the generation of stable and uniform current, the reaction rate can be tailored by the solution temperature to balance the Nb oxidization and Nb_2O_5 dissolution.[11,14]

Despite the understanding of the general mechanism, a quantitative and comprehensive understanding of the relationship between the processing parameters and the electrochemistry of the SRF cavity is still lacking. The challenge lies in the fact that there are several factors acting synergistically and impeding the uniform metal dissolution and oxidation over increasingly complicated geometries. Firstly, due to the difference in distance between the cathode and anode caused by the geometry of the cavity, the secondary current distribution is non-uniform and difficult to measure and control experimentally. Secondly, Joule heating induced during electrochemical polishing process will alter the temperature in the electrolyte, affect the kinetic parameters of the reactions, and ultimately lead to high ionic diffusion rate and local tertiary current density.[11] The variance in both secondary and tertiary current significantly complicate the problem. This will result in poor polishing result due to the formation of pits and porous oxide,[11] as well as the generation of bubbles produced during

---

[z] E-mail: caiw@vt.edu; huit02@jlab.org; reece@jlab.org

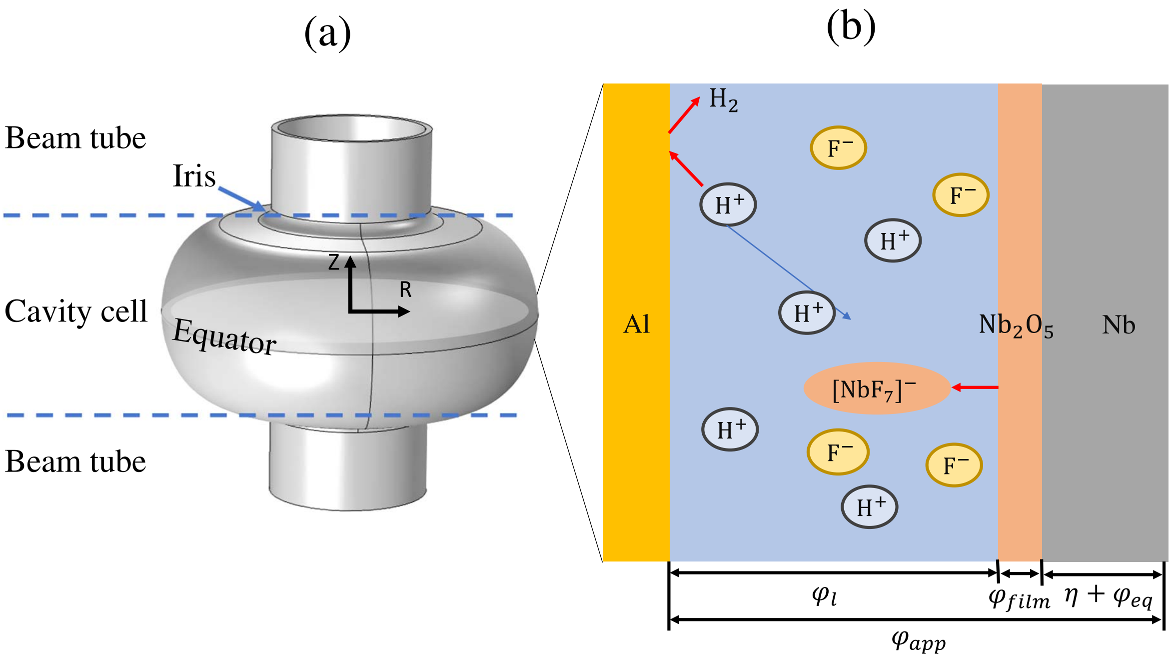

Figure 1. Schematic of the (a) 3D geometry of the C100 Nb cavity, and (b) electrochemical mechanisms during EP of Nb in hydrofluoric-sulfuric acid electrolyte.

reactions, all of which impede local ionic diffusion to cause non-uniform electrochemical polishing in microscale.[18] In addition, high dissolution rate caused by high temperature will cause the protecting oxide layer to completely dissolve, exposing the Nb surface directly to the acidic environment, leading to etching instead of uniform electrochemical polishing to the metal surface.[9] Lastly, the non-uniform temperature distribution will also affect the uniformness of the current distribution in macroscale, compromising the polishing results.[19]

To address the above challenges and complexity during electrochemical polishing of Nb cavities, this work aims to develop a numerical modeling framework that couples the complex cavity geometry, and the multiphysics nature of the electrochemical polishing process, which includes the electrochemical reactions, thermal effects and fluid flow of the electrolyte and coolant, to systematically investigate the synergistic effects of electrochemical polishing conditions and cavity geometry on the metal dissolution kinetics. While several work has been done in the past using the finite element (FE) method to study the separate effects of fluid dynamics[20] or cavity geometry,[21] little work has been done to evaluate their synergistical effects using experimental results as validations. In this project, a multiphysics FE model was developed to simulate the electropolishing kinetics using simple coupon geometry and validated by the experimental potentiodynamic results. The electropolishing kinetics were further applied to a C100 one-cell cavity geometry (as shown in Fig. 1a). The current distribution, temperature and oxide thickness distribution along the cavity surface was simulated. Using this model, the effects of coolant flow and temperature on the surface current and oxide thickness was studied. The model paves the way for further investigation of electrochemical polishing of new cavity geometry (for example, the RFD crab cavity[22]) and the design for cooling systems that could greatly expedite future accelerator design and manufacture.

Experimental and Modeling Methods

Experimental methods.—Electrochemical tests were conducted using standard 3-electrode setup, with the rectangular coupon of Nb with 0.6 cm^2 exposed area used as the working electrode (WE), Al plate as the counter electrode (CE), and mercury/mercury sulfate standard electrode as the reference electrode (RE). The electrolytes were a mixture of analytic grade 49% hydrofluoric acid and 96% sulfuric acid with volume ratio of 1:10, which is the same electrolyte used in electrochemical polishing. Potentiodynamic polarization curves of Nb were measured by a potentiostat (Gamry, PA, USA) with a potential ranging from -1 V to 1 V with respect to the RE from 10 °C–45 °C. The electrochemical parameters reflecting the kinetics of the cell, including equilibrium potential, corrosion current density and transfer coefficient was obtained from the potentiodynamic curve. The plateau current density is also measured as a function of the temperature. The test was run with static electrolyte with any stirring and the system was kept in a water bath to control the temperature.

Finite element models.—COMSOL Multiphysics (version 5.3) was used for the FE models, with simulation and validation steps as shown in Fig. 2. The built-in fully coupled solver with automatic highly non-linear Newton iteration method was applied for the simulations. The minimum damping factor is set to be 10^{-6} and a relative tolerance of 0.001 is given for the solver. Triangular shaped meshes are applied throughout the model, as shown in Figs. 3c, 3d. A coupon model with simple geometry were first simulated to investigate and validate the proposed electrochemical mechanism of the electrochemical polishing process. The potentiodynamic curve was simulated by the coupon model and compared to that obtained from the experiments to validate the i-V relationship. Then the electrochemical setup was applied to a model using the C100 cavity geometry with added effects of temperature and coolant flow.

Coupon model geometry.—The coupon sample model simulated the scenario where two flat rectangular electrodes of Nb (anode) and Al (cathode) were placed in parallel to each other in the electrolyte, as shown in Fig. 3a. To avoid the complexity of the convergence problem caused by the edge effect and focus only on the surface kinetics, the geometry was simplified as two parallel surfaces with the rectangular-shaped electrolyte of 5 × 10 cm^2 between them. The right boundary of the rectangle is the Nb sample surface, which is assigned with the Butler-Volmer kinetics, faradaic oxide growth and

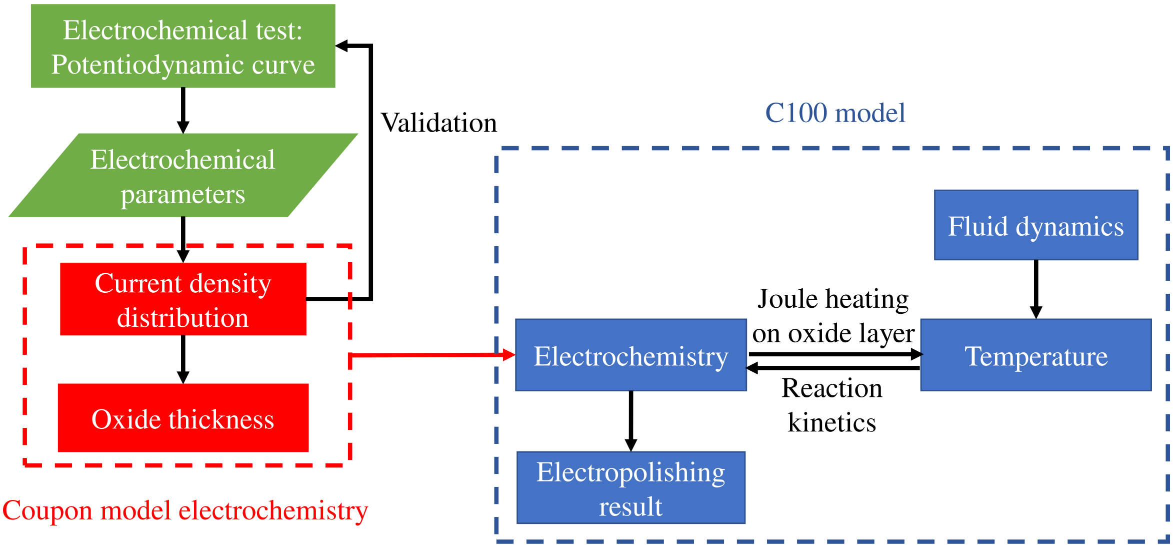

Figure 2. Flowchart of the developed FE modeling and experimental validation schemes.

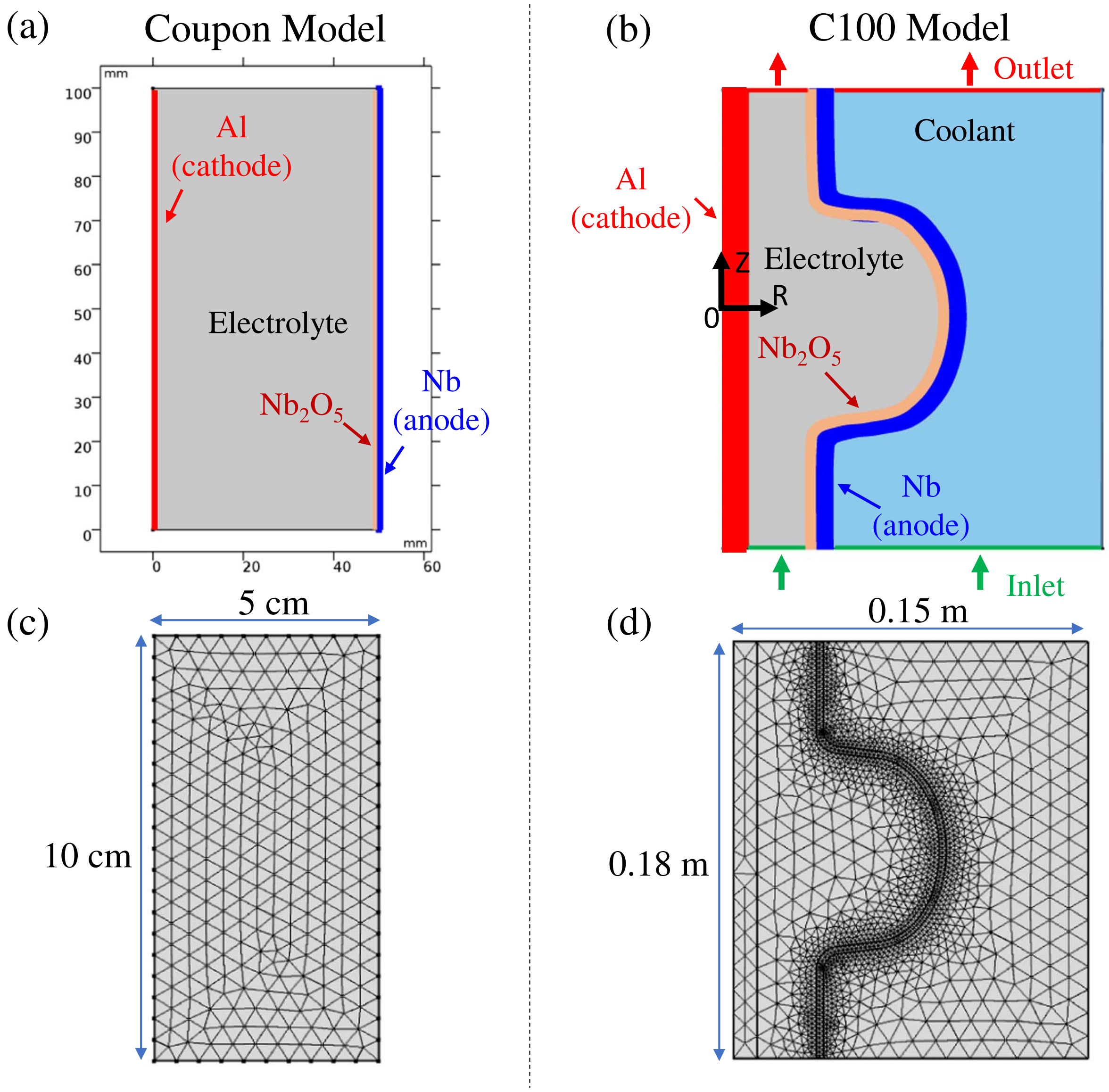

Figure 3. (a)–(b) FE model setup schematics and (c)–(d) meshing plot for the coupon and C100 models.

non-faradaic dissolution as described in the next section. The left boundary is the Al counter electrode surface with the Butler-Volmer kinetics to reflect the hydrogen evolution reaction. The meshing size of the coupon model is 5 mm.

Coupon model governing equations.—The reaction kinetics of the oxidization of Nb in the low voltage region is given by the Butler-Volmer equation:

$$i_{B-V} = i_0\left(\exp\left(\frac{\alpha_a F\eta}{RT}\right) - \exp\left(\frac{\alpha_c F\eta}{RT}\right)\right), \qquad [4]$$

where i_0 stands for the equilibrium corrosion current density, α_a and α_c stands for the anodic and cathodic transfer coefficient respectively, and η stands for the overpotential. The overpotential η is defined as

$$\eta = \varphi_{app} - \varphi_l - \varphi_{film} - \varphi_{eq}, \qquad [5]$$

in which φ_{app} is the externally applied potential, φ_l is the electrolyte potential at the interface, φ_{film} is the potential drop from the metal (hydr)oxide layer, and φ_{eq} is the equilibrium corrosion potential. When the overpotential is much higher or lower than 0, the Butler-Volmer equation could be approximately simplified to Tafel equation. The transfer coefficient α could be correlated with the Tafel slope β by equation

$$\alpha = \frac{2.303RT}{F\beta} \qquad [6]$$

To simulate the circumstance when the applied potential drives the system to the plateau region, the equation is implemented to calculate the local corrosion current density:

$$i_{loc} = \frac{i_{B-V}}{1 + \dfrac{i_{B-V}}{i_{lim}}}, \qquad [7]$$

where i_{lim} is the limiting current density. This Eq. 7 ensures the smooth transition of the potentiodynamic curve from Butler-Volmer region to plateau region. At the Butler-Volmer region where $i_{B-V} \ll i_{lim}$, it is assumed that $i_{loc} \approx i_{B-V}$. At the plateau region where $i_{B-V} \gg i_{lim}$, it is assumed that $i_{loc} \approx i_{lim}$. Here the i_{lim} is assumed to be the same as the temperature-dependent plateau current density as measured by the experiment, which is listed in Table III.

The growth rate of oxide per reaction[1] is implemented by the following equation

$$\mathrm{v_F} = \frac{\nu \mathrm{i_{loc}M}}{\mathrm{nF}\rho}, \qquad [8]$$

where $\mathrm{v_F}$ is the growth rate expressed in thickness/time, ν is the stoichiometric coefficient, which is 1, $\mathrm{i_{loc}}$ is the current density calculated using Eq. 7, M is the molar mass of the niobium pentoxide, which is 0.26581 kg mol^{-1}, n is the electron transferred during the reaction, which is 5, F is the Faraday's constant, and ρ is the density of the niobium pentoxide, which is 4550 kg m^{-3}.

Apart from the Faradaic oxide growth described above, the oxide dissolution reaction expressed by reaction[3] happens in a non-Faradaic manner. Such reaction does not induce electron transport between the Nb anode and Al cathode and thus does not contribute to the overall current density. The rate of this reaction is determined by the concentration of H^+ and F^- that could reach the surface of the Nb_2O_5. Compared to the F^- ions, H^+ ions has a much higher concentration in this acidic electrolyte composed of the mixture of HF and H_2SO_4, so the main rate limiting factor of this reaction is the diffusion of F^- ions.[23] The non-faradaic dissolution rate $\mathrm{v_{NF}}$ is given by

$$\mathrm{v_{NF}} = (\mathrm{DMc_{F^-}})/(\rho\delta), \qquad [9]$$

where D is the temperature-dependent diffusion coefficient of F^- ions as listed in Table I,[16] c_{F^-} is the concentration of F^- ions and δ is the thickness of the diffusion layer. In our study, a concentration gradient of 25,701,254 mol m^{-4} is used as a replacement of the $\mathrm{c_{F^-}}/\delta$ term, obtained based on the result from Ref. 16.

Table I. Summary of diffusion coefficient of F^- ions under different temperatures (T) interpolated from the experimental data from Ref. 16.

T (°C)	D ($\times 10^{-12}$ m^2 s^{-1})
1	2.69
9	4.86
19	8.77
30	12.9
41	28.3
50	29.0

Thus, the total growth rate ($\mathrm{v_n}$) of the oxide is then given by

$$\mathrm{v_n} = \mathrm{v_F} - \mathrm{v_{NF}} = \frac{\nu \mathrm{i_{loc}M}}{\mathrm{nF}\rho} - \mathrm{v_{NF}}. \qquad [10]$$

By integrating the growth rate with respect to time, the thickness of the Nb_2O_5, as well as the resistance of the oxide could be obtained as

$$r_{film} = \frac{\int v_{\mathrm{n}}\,\mathrm{dt}}{\sigma} \qquad [11]$$

where σ is the electrical conductivity of niobium pentoxide, which is 1.46×10^{-6} S m^{-1}.[24,25] The φ_{film} defined in Eq. 5 is then calculated from r_{film} along the cavity surface using Ohmic law

$$\varphi_{film} = \mathrm{i_{loc}} r_{film} \qquad [12]$$

C100 model geometry.—A 2D axisymmetric model was built for the C100 cavity, as shown in Fig. 3b. The wall thickness of the Nb cavity is 3 mm. The counter electrode is an aluminum rod. The internal of the cavity is filled with electrolyte, while the outside by the coolant (i.e. water). The diameter of the chamber for outside water cooling is 0.15 m, giving an inlet area of 0.0661 m^2. The size of the inlet for inside electrolyte flow is 0.00353 m^2. The meshing of the C100 model is finer near the Nb surfaces than elsewhere so that the potential, current density and temperature distribution have larger gradient near the boundary of the Nb cavity. The meshing size near and inside the cavity wall is set to be 2 mm and slowly transitions to 10 mm in regions far from the wall, as plotted in Fig. 3d.

C100 model governing equations.—The electrochemical kinetics for C100 model was set up the same as the coupon model. The coupling of temperature with faradaic oxidization was implemented by the temperature-dependent limiting current density $\mathrm{i_{lim}(T)}$, interpolated from the experimental data as listed in Table III, while the non-faradaic dissolution rate was calculated based on the temperature-dependent diffusion coefficient of F^- ions in the electrolyte, interpolated from the experimental data as listed in Table I.[16]

The inlet and the outlet of the coolant flow direction is shown in Fig. 3b. The electrolyte flows into the cavity while the outside is filled with cooling water flow. Both the inside and the outside flows are given laminar flow conditions and are set to be fully developed flow. The boundary condition of the fluid is set as no slip, meaning that fluid velocity at the wall is zero. The boundary condition of the inlet of the inside electrolyte flow is given by a total flow rate of 1 gallon $\min^{-1}$. For outside water coolant, three coolant flow rates, 1, 10 and 100 gallon $\min^{-1}$. (GPM), were chosen to represent a mild, average, and aggressive coolant flow strategy.

The general heat transfer is governed by the equation

$$\rho C_p \frac{\partial T}{\partial t} + \rho C_p u \cdot \nabla T + \nabla \cdot (k \nabla T) = Q, \qquad [13]$$

where ρ is the density of the material or liquid, C_p is the heat capacity at constant pressure, T is the temperature, t is the time, k is the thermal conductivity, and Q is the heat source power per unit area, given by Joule heating of the oxide layer as

$$Q = {i_{loc}}^2 r_{film}. \qquad [14]$$

Because the conductivity of the Nb, Al metal and the electrolyte is much larger than that of the niobium pentoxide, thus, Joule heat generated by similar current flowing through them is negligible comparing to that of the niobium pentoxide and not considered in this model. The outside boundary of the system is set to be an open boundary for heat transfer.

Results and Discussion

Potentiodynamic polarization behavior of Nb.—The experimentally measured potentiodynamic polarization curve of Nb in hydrofluoric-sulfuric acid electrolyte at 20 °C is plotted in Fig. 4a. The curve could be separated into a Butler-Volmer region at low potentials (∼−1.25 V to −0.5 V vs Hg/Hg_2SO_4) and a plateau region at high potentials (∼−0.5 V to 1.0 V vs Hg/Hg_2SO_4). It can be seen that the equilibrium corrosion potential is ∼−0.823 V vs Hg/Hg_2SO_4. The transfer coefficient of the anodic and cathodic branches listed in Table II were calculated from Eq. 6 using the anodic and cathodic Tafel slopes obtained by linear fitting of the curves within ± 200 mV of the open circuit potential, as denoted by the blue and red solid lines respectively in Fig. 4a. The equilibrium corrosion potential and current density was determined at the intersection of the two Tafel lines. The obtained parameters are also listed in Table II and used for the FE simulations. The limiting current density (i_{lim}) is obtained from the plateau region by the average value of the current density at 0 V, 0.5 V and 1 V. The limiting current density was measured for different temperatures and the result is listed in Table III. The temperature deviation during the measurement of the potentiodynamic curve is kept below 1.5 °C for each data point. It can be seen from Fig. 4b that the limiting current density increased monotonically with temperature, from ∼8.4 mA cm^{-2} at 10 °C to ∼ 40 mA cm^{-2} at 45 °C, similar to the trend reported by Jin et al.[26]

Table II. Summary of the electrochemical kinetic parameters of Nb used in the FE simulations, where α, φ_{oc}, and i_0 represents the transfer coefficient, equilibrium corrosion potential, and equilibrium corrosion current density respectively, as defined in section 2.2.

	α	φ_{eq} (V vs Hg/Hg_2SO_4)	i_0 (mA cm^{-2})
Cathodic	−0.568	−0.823	4.61 × 10 − 2
Anodic	0.644		

Coupon model validation.—The experimentally measured electrochemical kinetic parameters listed in Table II were used as inputs for the FE coupon model. A potentiodynamic polarization curve was then simulated by the coupon model using the governing equations described in section 2.2, as shown in Fig. 4c. For the simulation, after applying different potentials, the average current density flow through the surface were calculated using the model. Figure 4c shows that the simulated curve successfully captured the shape of the potentiodynamic curve at the Bulter-Volmer region and the plateau region, demonstrating the validity of the electrochemical kinetics setup. The same electrochemical kinetics is then applied to the C100 model.

Electrochemcial behavior of C100 Nb cavity.—*Surface electrochemistry and Joule heating.*—During the simulation of C100 cavity (without and with coolant), the Nb surface was grounded (0 V vs RE) while the Al electrode was applied a fixed potential of—14 V vs RE. The simulated electrochemical polishing results of C100 cavity without coolant flow are summarized in Figs. 5–7. The inside of the cavity is filled with static (i.e. non-flowing) electrolyte and the outside of the cavity is static air. The outside boundaries of the air domain are set as open boundaries, which allows the outgoing heat flux if the temperature exceeds ambient temperature. It's worth noting that the coupling between electrochemistry and temperature is a positive feedback loop, which means that the electrochemical polishing current and the temperature in the vicinity areas will constantly go higher, at least in the range when the measured electrochemical kinetics data is valid. Without proper cooling, the system does not reach an equilibrium state. Thus, results from a few representative transient times are shown here. It should also be pointed out that, even though the results are presented in the order of temperature distribution followed by electrochemical status, these two processes affect each other back and forth in the electrochemical polishing process.

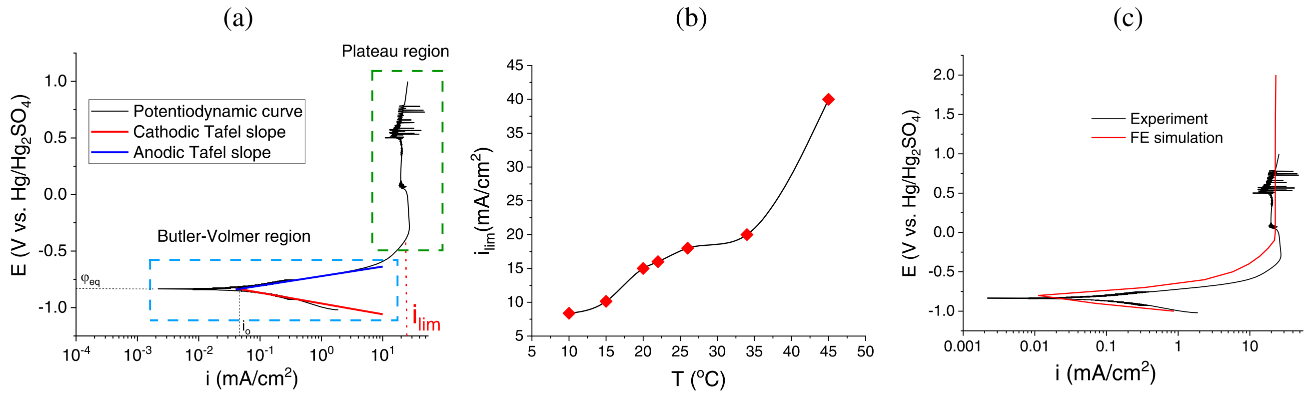

Figure 4. (a) Potentiodynamic polarization curve of Nb measured in hydrofluoric-sulfuric acid electrolyte at 20 °C. (b) Summary of the experimentally measured limiting current density as a function of temperature. (c) Simulated and experimentally measured potentiodynamic polarization curves of Nb in hydrofluoric-sulfuric acid electrolyte at 20 °C.

Table III. Summary of limiting current density under different temperatures (T) measured by potentiodynamic polarization tests.

T (°C)	i_{lim} (mA cm^{-2})
10	8.37
15	10.13
20	15.32
22	16.26
26	18.15
34	20.64
45	40.01

Figures 5a–5c demonstrates the temperature distribution of the system at 1 min, 5 min and 30 min after the electrochemical polishing starts. The temperature at the inner surface of the cavity at these time steps is plotted in Fig. 5d. It can be seen that without the coolant flow, the system heats up quickly, from ~25.3–26.1 °C at 1 min, to ~32.4 °C after 30 min. It is also noted that due to the different heat capacity of the electrolyte and air, after 30 min of electrochemical polishing, the temperature is much higher in the air side (~32.4 °C) than that of the electrolyte (~24 °C), especially near the Al surface. Nonetheless, except for the initial 1 min, the temperature distribution along the Nb surfaces were found to be rather uniform.

The electrolyte potential and current density distribution within the electrolyte of the C100 cavity are shown in Fig. 6, where the different anode-cathode distance along the Nb surface results in rather localized electrochemical activities. Near the equator of the cell, the electrolyte potential was found to be much higher than that from regions far away, as shown in Figs. 6a–6c, indicating a different driving force for reaction. Figures 6d–6f shows the current distribution inside the electrolyte, where the current flow vectors (magnitude and direction) are represented by the arrows. It can be seen that along the Nb surface, a local high current density of ~50 mA cm^{-2} is observed near the iris regions of the cavity at 1 min, which increased to ~80 mA cm^{-2} at 30 min.

The accumulated oxide thickness and the surface current density through the Nb-electrolyte interface along the z direction are shown in Fig. 7. The current density as shown in Fig. 7b is the current density normal to the surface, which indicates the electropolishing rate. Note that this is different from the electrolyte current density magnitude from Figs. 6d–6f in the vicinity of the surface, which considers the current caused by potential gradient parallel to the surface. From these results, it could be seen that higher temperature will lead to higher reaction rate for both oxidization reaction and oxide dissolution reaction. The oxide thickness at 5 min is smaller

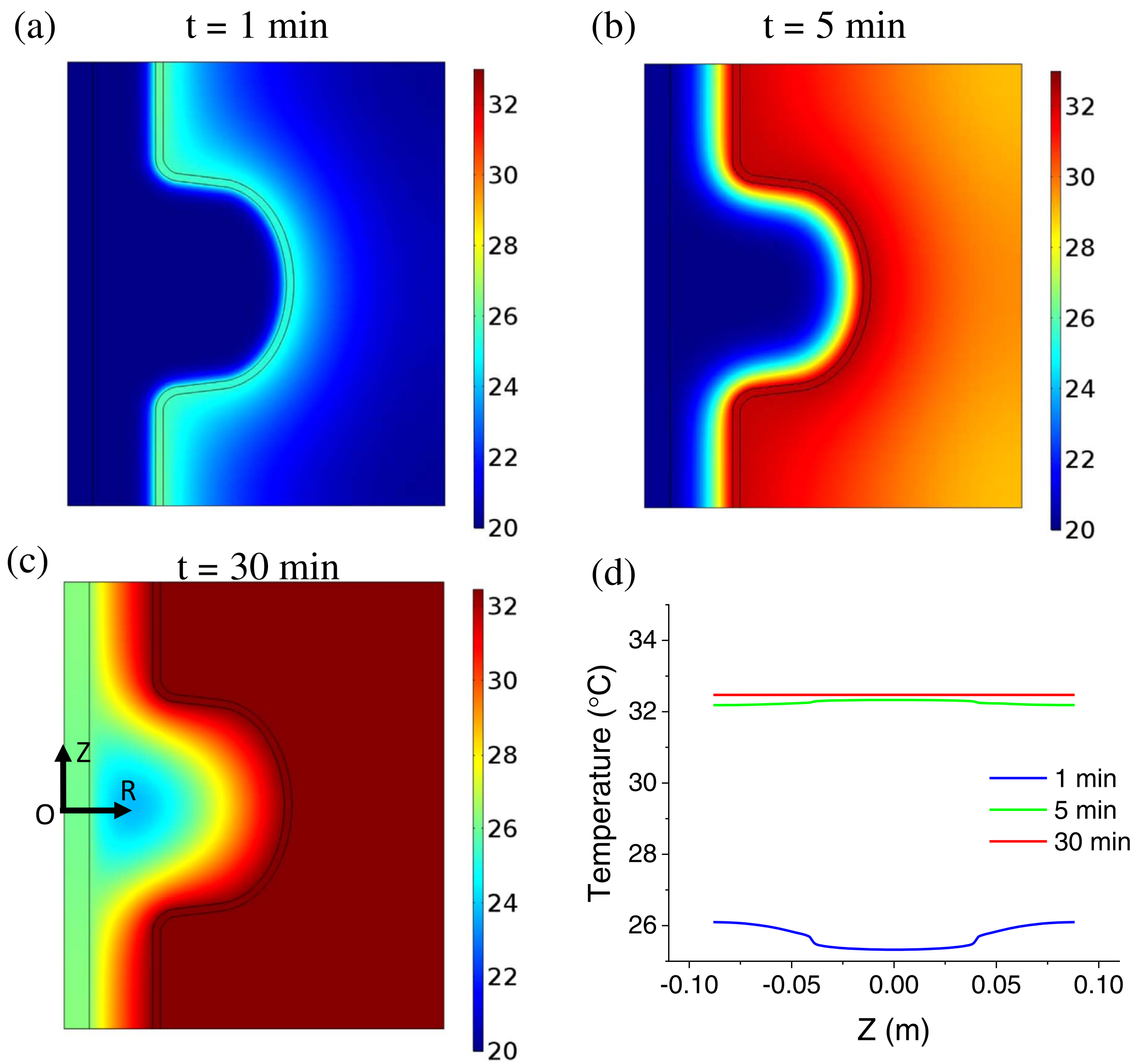

Figure 5. Simulated system temperature distribution without coolant flow at (a) 1 min, (b) 5 min and (c) 30 min, and (d) temperature profile along the inner surface along the z-direction as defined in Fig. 2b.

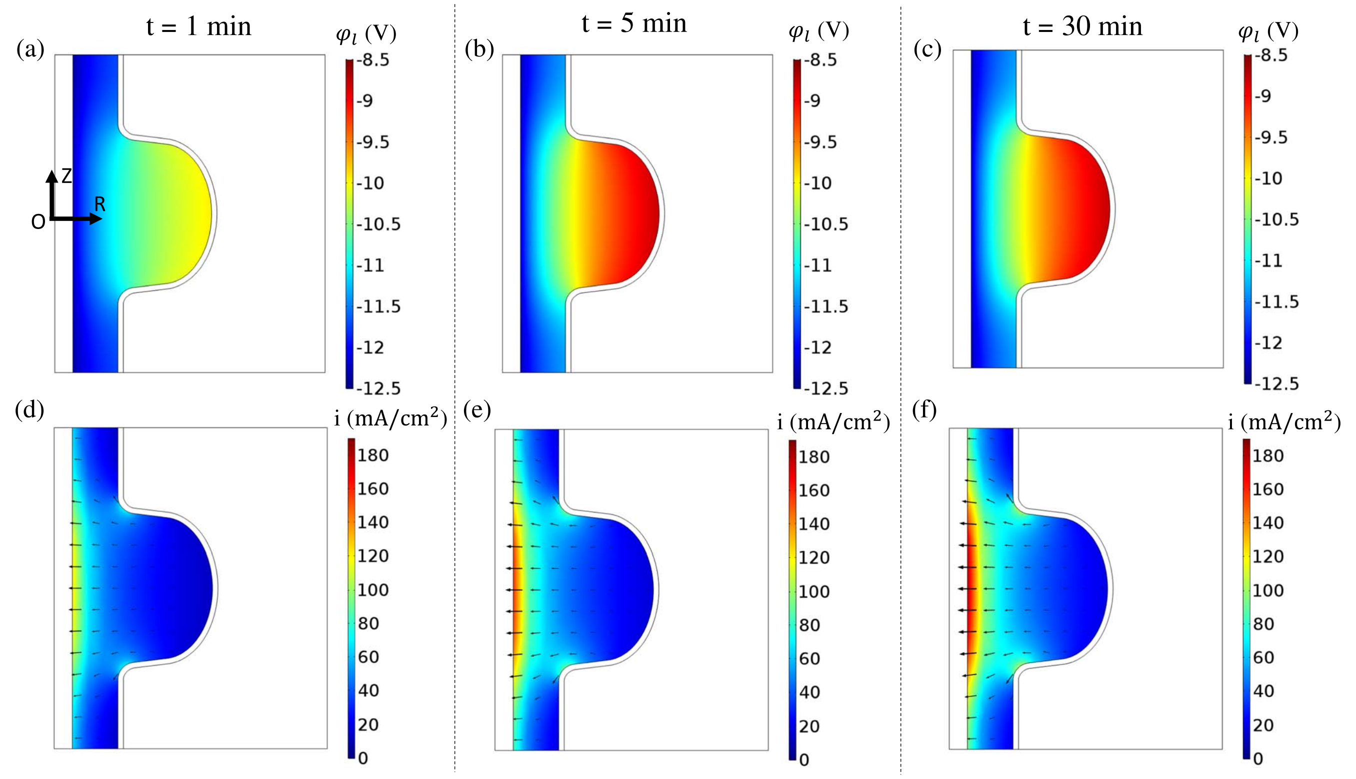

Figure 6. Simulated electrolyte (a)–(c) potential and (d)–(f) current density distribution without coolant flow after (a), (d) 1 min, (b), (e) 5 min, and (c), (f) 30 min of EP.

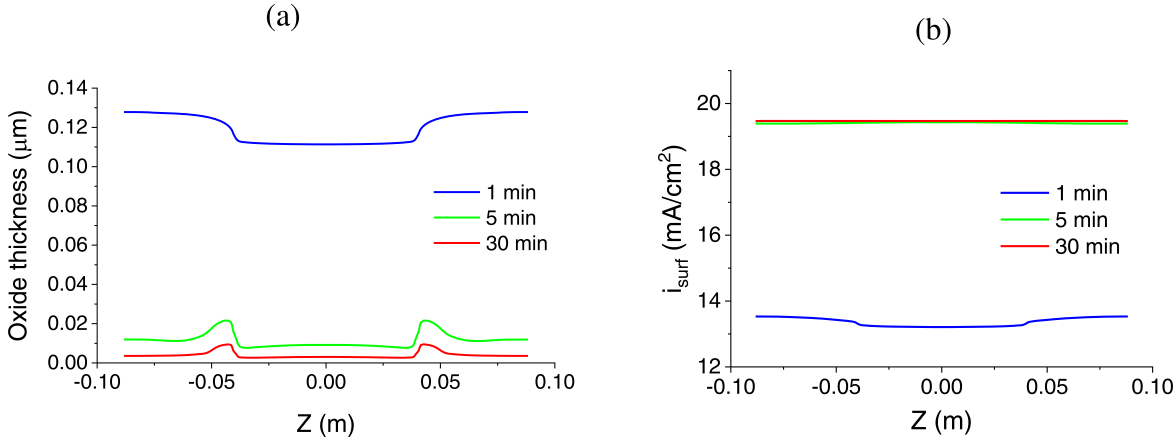

Figure 7. Simulated (a) oxide thickness and (b) current density distribution along the surface of the Nb cavity.

than that at 1 min and keeps on decreasing. This indicates that the dissolution rate increases with temperature faster than the oxidation rate. These simulated results thus show that without sufficient cooling, the high temperature generated from electrochemical polishing of just 5 min will quickly dissolve the majority of the anodized oxide, which is likely to cause subsequent etching of the metal surface, resulting in undesirable rough metal surface. The non-uniform oxidation and dissolution rate also leads to a hump at the iris region. At first, the fast oxidation rate caused by geometry at beam tube region together with the iris region is dominant comparing to the dissolution rate which leads to thicker oxide. As the temperature of the whole system rises, the fast dissolution rate becomes dominant at the beam tube, so the iris region is left with thicker oxide than the beam tube and the equator region. In addition, such high temperature could also lead to the formation of porous oxide layer (instead of dense and compact oxide layer) and large amounts of hydrogen bubbles to further deteriorate the polishing results. These simulated results thus highlight the necessity of thermal management during the electrochemical polishing process to achieve an optimized surface finish.

Effects of coolant on surface electrochemistry.—Figures 8–10 demonstrates the results of the C100 model with coolant. We started with no oxide at first. At the first few minutes, the current density is high and the oxide grows thicker. During this time, Joule heating is high and will raise the temperature of the system. However, as the oxide grows thicker, the current density drops and Joule heating power begins to decrease. With sufficient coolant flow, the cooling and the heating of the system was found to reach an equilibrium. The oxidization of Nb and dissolution of its oxide also reached an equilibrium and resulted in a steady electrochemical polishing state. Three outside coolant flow rates, 1, 10 and 100 gallon min^{-1}.

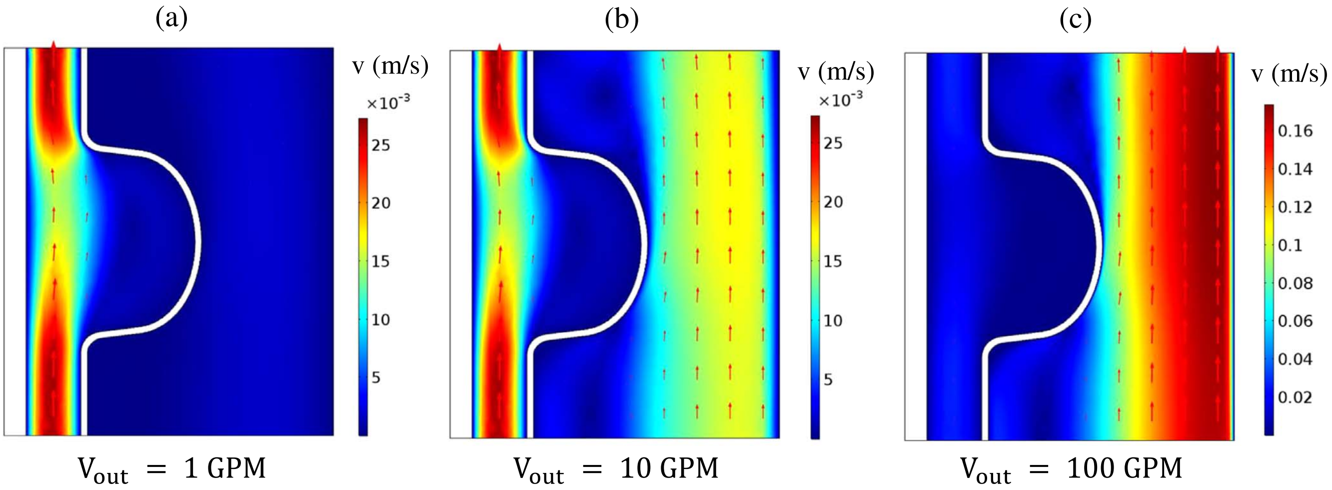

Figure 8. Simulated flow velocity distribution of the electrolyte and coolant water flow with a coolant flow rate of (a) 1, (b) 10, and (c) 100 GPM.

(GPM), were chosen to represent a mild, average, and aggressive coolant flow strategy. The inside electrolyte flow was set to be 1 GPM for all the circumstances. Figure 8 shows the fluid dynamics of the three different flow rates under the influence of the cavity geometry. It could be seen that the electrolyte flow is faster at the beam tube area while slower at the cavity cell region, thus providing a more significant cooling effect on the beam tube area. The coolant flow (outside of the tube), on the other hand, is rather stagnant at the beam tube region, so it cools down the cavity cell region more effectively. Thus, both inside electrolyte and outside coolant flow are essential for achieving a uniformly low temperature of the system to maintain a steady and uniform electrochemical polishing rate along the Nb cavity surface.

Based on the actual cooling capability of Jefferson Lab,[27] two inflow fluid temperatures, 7 °C and 20 °C, were chosen for both the inside electrolyte flow and outside water flow. As shown in Fig. 9, with the coolant flow, the system temperature is lowered for all coolant setups studied, with more significant cooling at higher GPM. An asymmetrical temperature distribution could be observed because of the direction of the flow. Because the low velocity of the

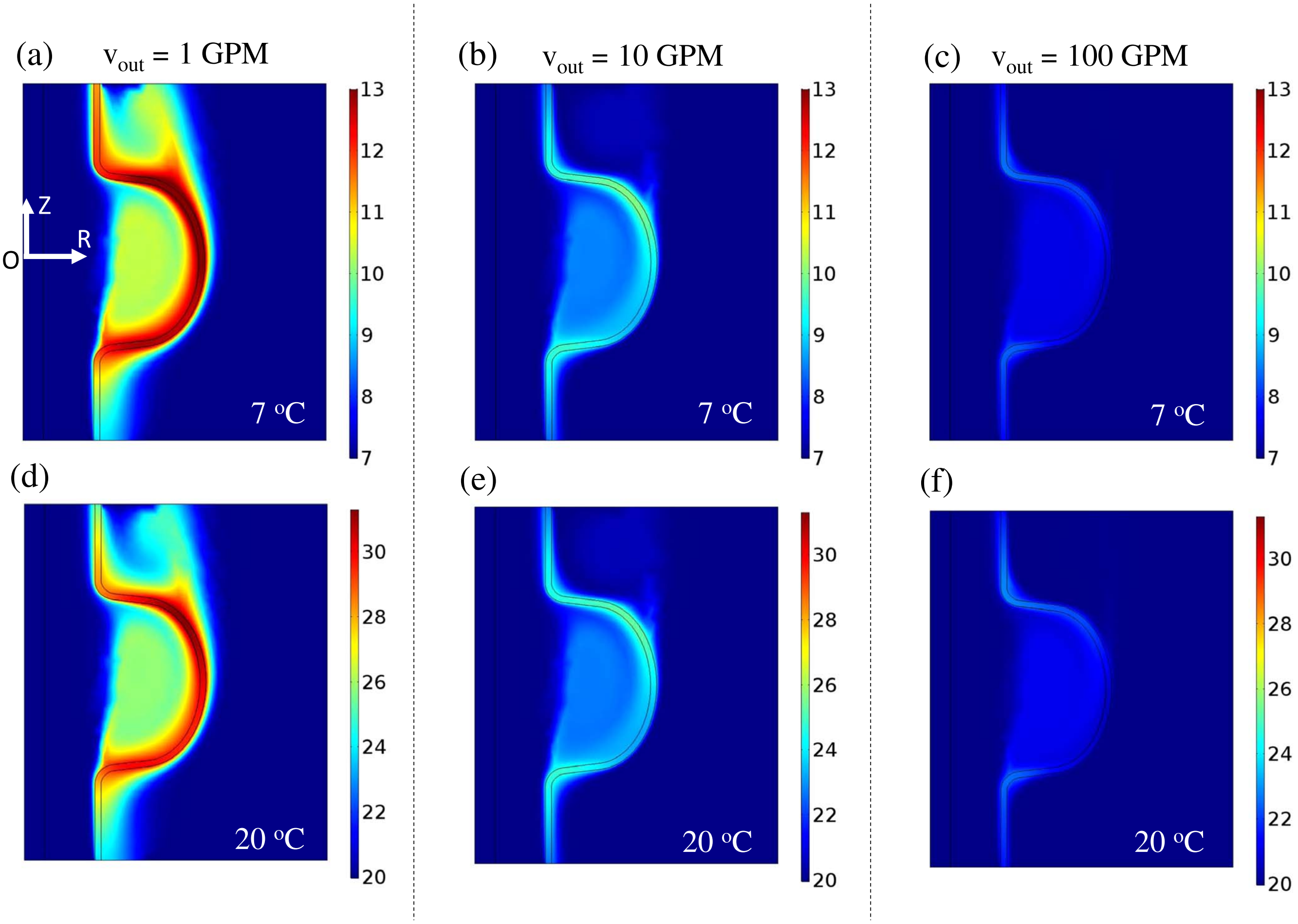

Figure 9. Simulated temperature distribution with different coolant flow of 1–100 GPM at (a)–(c) 7 °C and (d)–(f) 20 °C coolant temperature.

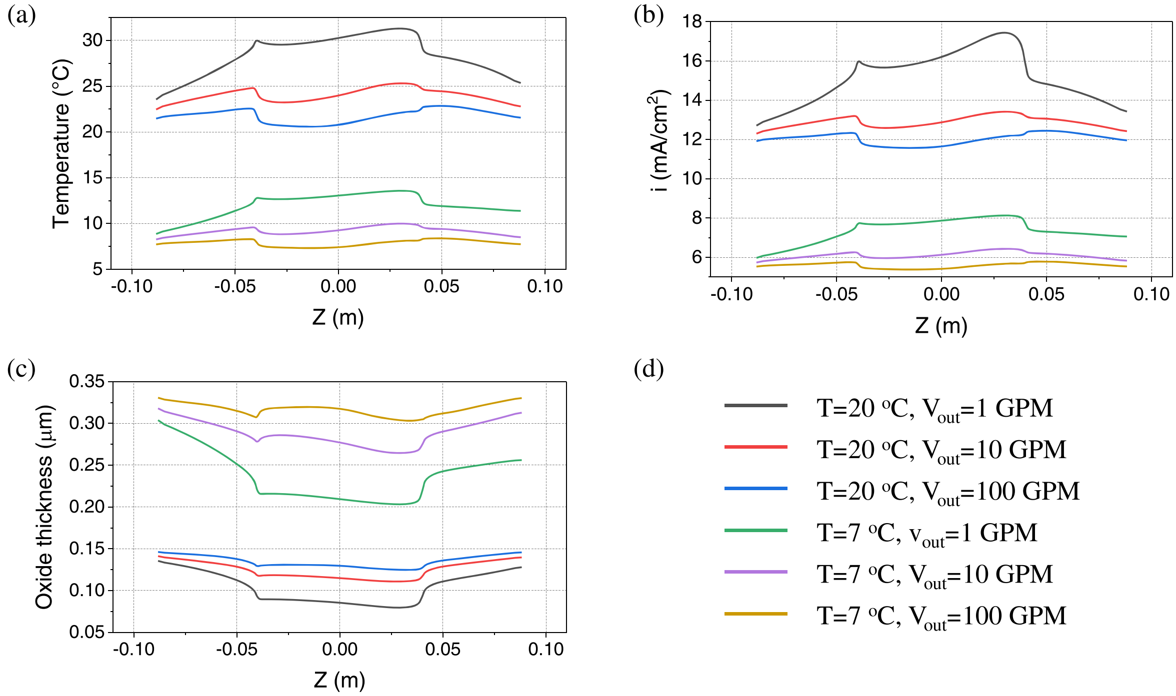

Figure 10. Simulated (a) surface temperature, (b) surface corrosion current density, and (c) oxide thickness under different cooling conditions as listed in the color legend in (d).

inside electrolyte flow, a high temperature area could be observed in the cavity cell region. Another high temperature region could be seen at the upper half of the cell region, due to the stagnant flow of the outside coolant. It is also noticed that at 10 and 100 GPM, the upstream cavity wall (i.e. regions closer to the incoming flow) gets more effective cooling than other regions. Figure 10a shows the temperature profiles at the inner surface of the cavity. It could be seen that, for both 7 °C and 20 °C coolant, the flow rate of 1 GPM is not enough to provide efficient cooling at the cavity cell region and the downstream beam tube region. A coolant flow rate of 100 GPM, on the other hand, would cause over-cooling at the cell region, which lead to even higher temperature variance of Nb than that from 10 GPM (Fig. 10a). In addition, the simulated current distribution in Fig. 10b also confirms that 10 GPM flow is the optimal choice for the electrochemical polishing process, that results in the least current variation along the surface. As for the coolant temperature, the 7 °C coolant was found to maintain the system at an even lower temperature, keeping the electrochemical polishing current at a lower value with smaller variance than those at 20 °C. This is expected to allow the formation and dissolution of the oxide layer to proceed at a low rate, leading to smoother surface finish. The simulated results for oxide thickness are plotted in Fig. 10c. Even though the oxide thickness variation is not the smallest for the optimal coolant setup, which is 7 °C and 10 GPM, it is not the key parameter to determine polishing result as long as it is thick enough to prevent etching. Thus, based on these simulation results, it is concluded that among all conditions studied, 7 °C coolant inflow temperature with 10 GPM flow rate is the optimal electrochemical polishing condition, providing sufficient cooling with an achievable flow rate to allow the generation of rather uniform surface current and oxide thickness.

Discussions on model limitations.—Despite the success in simulating the current and potential distribution, oxide growth kinetics of Nb electropolishing in a complex cavity geometry under different cooling setups, the model still has several limitations. Firstly, the model doesn't consider the effect of electrolyte flow velocity on ion concentration, which could affect the diffusion limited current density. This is limited by the discrepancy in length scale between the diffusion layer, which is a few μm, and the general geometry of the cavity, which is tens of cm. However, fresh electrolyte flowing in the cavity will only benefit the electropolishing quality and does not affect the significance of the results predicted by our model. Another limitation is that the model hasn't taken convection flow into account due to the instability it will induce into the coupling between the temperature and fluid dynamics. The temperature gradient in this circumstance is small and the convection flow it generates could be neglected compared to the active coolant flow. Nonetheless, a model with the ion transport under the effect of flow and the fluid dynamics considering the convection flow is needed in the future to accommodate the model to more scenarios and improve the model's precision. The model could also benefit from more experimental validation on the oxide thickness in future studies, which could be conducted to calibrate the oxide growth kinetics.

Conclusions

In this work, a FE multiphysics model was built and assisted by experimental methods to investigate the electrochemical polishing kinetics of Nb for applications in SRF cavities. Experimentally, it was found that the polarization behavior of Nb in hydrofluoric-sulfuric acid electrolyte shows a Butler-Volmer region at low potentials (~ -1.25 V to -0.5 V vs Hg/Hg_2SO_4) and a plateau region at high potentials, with the limiting current density in the plateau region increasing monotonically with temperature from 10 °C–45 °C. Using the experimentally validated FE model, the effects of Joule heating, temperature, coolant flow rate on the uniformity of surface current density and oxide thickness along the curved Nb walls of a C100 cavity was studied. It was found that without coolant, the Joule heating quickly accelerate oxidation dissolution, leading to an ultra-thin oxide layer and unfavorable high surface current density on Nb surface. On the other hand, when coolant was applied, its temperature and flow rate were found to significantly affect the surface current distribution and oxide uniformity. Among all conditions studied, an optimum coolant setup of 7 °C and 10 GPM was identified. This developed modeling framework could be used to provide fast and high-fidelity simulations of Nb surface electrochemistry as a function of processing conditions for future cavity design and manufacture, which would be otherwise expensive and time-consuming to perform experimentally.

Acknowledgments

This research was financially supported by the US Department of Energy Thomas Jefferson National Accelerator Facility. This material is based upon work supported by the U.S. Department of Energy, Office of Science, Office of Nuclear Physics under contract DE-AC05–06OR23177. The computational resource used in this work is provided by the advanced research computing (ARC) at Virginia Polytechnic Institute and State University. KW greatly appreciated help and advice from Gary Chen, Jim Henry, Anne Marie Valente, and Subashini De Silva from Jefferson Lab for discussion of the results.

ORCID

Wenjun Cai https://orcid.org/0000-0002-9457-8705

References

1. C. E. Reece, *Phys. Rev. Accel. Beams*, **19**, 124801 (2016).
2. G. Ciovati, “Review of high field Q slope, cavity measurements.” *Proceedings of SRF2007* (Beijing, China) (2008).
3. L. Lilje, *Experimental Investigations on Superconducting Niobium Cavities at Highest Radiofrequency Fields* (University of Hamburg, Hamburg, Germany) 127 (2001).
4. G. Ciovati, H. Tian, and S. G. Corcoran, *J. Appl. Electrochem.*, **41**, 721 (2011).
5. T. Hryniewicz, K. Rokosz, and H. R. Z. Sandim, *Appl. Surf. Sci.*, **263**, 357 (2012).
6. M. Sowa et al., *Mat Sci Eng C-Mater*, **42**, 529 (2014).
7. A. W. Hassel and D. Diesing, *Thin Solid Films*, **414**, 296 (2002).
8. L. Neelakantan, A. Pareek, and A. W. Hassel, *Electrochim. Acta*, **56**, 6678 (2011).
9. H. Tian, S. G. Corcoran, C. E. Reece, and M. J. Kelley, *J. Electrochem. Soc.*, **155**, D563 (2008).
10. T. R. Mandula and R. Srinivasan, *J Solid State Electr*, **21**, 3155 (2017).
11. A. Chandra, M. Sumption, and G. S. Frankel, *J. Electrochem. Soc.*, **159**, C485 (2012).
12. M. Inman, E. J. Taylor, and T. D. Hall, *J. Electrochem. Soc.*, **160**, E94 (2013).
13. M. Inman, E. J. Taylor, and T. D. Hall, *J. Electrochem. Soc.*, **163**, X5 (2016).
14. L. Guan, Y. Li, G. Wang, Y. K. Zhang, and L. C. Zhang, *Electrochim. Acta*, **285**, 172 (2018).
15. H. Tian, C. E. Reece, M. J. Kelley, and S. G. Corcoran, *13th Workshop on RF Superconductivity*, Beijing, China (2008).
16. H. Tian and C. E. Reece, *Phys Rev Spec Top-Ac*, **13**, 083502 (2010).
17. A. C. Crawford, *Nucl Instrum Meth A*, **849**, 5 (2017).
18. S. J. Lee, Y. H. Chen, and J. C. Hung, *Int J Electrochem Sc*, **7**, 12495 (2012).
19. D. Landolt, P. F. Chauvy, and O. Zinger, *Electrochim. Acta*, **48**, 3185 (2003).
20. C. E. Reece, J. Ortega, and J. Mammosser, *Proceedings of SRF2007*, Beijing, China (2008).
21. A. P. Rodríguez and L. M. A. Ferreira, p. 1 (2017), https://www.comsol.com/paper/download/440591/perez%20rodriguez_paper.pdf.
22. B. Xiao, J. Delayen, S. De Silva, Z. Li, R. Rimmer, S. Verdu-Andres, and Q. Wu, *HOM Damper Design for bnl EIC 197MHZ Crab Cavity* (Brookhaven National Lab. (BNL), Upton, NY (United States)) (2021).
23. F. Eozenou, S. Berry, C. Antoine, Y. Gasser, J. P. Charrier, and B. Malki, *Phys Rev Spec Top-Ac*, **13**, 083501 (2010).
24. R. A. Rani, A. S. Zoolfakar, A. P. O’Mullane, M. W. Austin, and K. Kalantar-Zadeh, *J. Mater. Chem. A*, **2**, 15683 (2014).
25. Y. T. Ravikiran, M. T. Lagare, M. Sairam, N. N. Mallikarjuna, B. Sreedhar, S. Manohar, A. G. MacDiarmid, and T. M. Aminabhavi, *Synthetic Met*, **156**, 1139 (2006).
26. S. Jin, X. Y. Lu, L. Lin, A. T. Wu, and K. Zhao, *Phys Rev Spec Top-Ac*, **13**, 061001 (2010).
27. C. E. Reece, *JLAB-TN-20-028* (2020).